PHYSICAL REVIEW B VOLUME 48, NUMBER 14 1 OCTOBER 1993-II

X-ray-absorption studies of zirconia polymorphs. I. Characteristic local structures

Ping Li and I-Wei Chen
Department of Materials Science and Engineering, University of Michigan, Ann Arbor, Michigan 48109-2136

James E. Penner-Hahn
Department of Chemistry, University of Michigan, Ann Arbor, Michigan 48109-1055

(Received 10 March 1993; revised manuscript received 28 May 1993)

Characteristic extended x-ray-absorption fine structure and x-ray-absorption near-edge structure spectra of zirconia polymorphs (monoclinic, orthorhombic, tetragonal, and cubic) have been identified at 10 K. For the host cations, these spectra are phase dependent but dopant independent because the dopant perturbation is short ranged. In the tetragonal structure, the first Zr-O shell is bifurcated into two tetrahedra, with outer O ions loosely bound and severely distorted. Although the tetragonal Zr cation network is nearly fcc and higher-order Zr-Zr coordinated shells are resolvable at distances up to 9 Å, other evidence points to incoherent-distortion reflecting phase instability. In monoclinic, orthorhombic, and cubic structures, a similar Zr-O polyhedron with sevenfold coordination and a comparable bond length is observed, along with a large distortion or splitting of the next-nearest-neighbor Zr-Zr shell. Progressive departure from the ideal fluorite structure by reducing the Zr-O coordination and dilating or distorting the local Zr-Zr network is seen to be correlated to increased phase stability but not to long-range crystal symmetry.

I. INTRODUCTION

Zirconia (ZrO_2) can form cubic, tetragonal, and monoclinic phases or orthorhombic phases at high pressures. A pressure-temperature phase diagram of pure zirconia polymorphs is given in Fig. 1 based on currently available thermodynamic and other schematic experimental data.[1-3] At room temperature, only the monoclinic form is stable, although both the tetragonal and orthorhombic phases can be quenched to ambient condition. Addition of appropriate dopants, however, is known to stabilize the tetragonal and cubic polymorphs. These partially (tetragonal) and fully (cubic) stabilized zirconia alloys have remarkable ionic and mechanical properties which have led to their applications as oxygen sensors, fuel cells, electrolytes, coatings, structural and wear components, and toughening agents in many ceramic composites. Consequently, much research has already been done on various aspects of these materials.[4-7] Despite such effort, the fundamental issues concerning the atomistic origins of phase stability, which is essential to their processing, properties, and applications as engineering materials, are still unresolved. Better characterization of the atomic and electronic structures of these ceramics could provide a basis for understanding phase stability. The present series of papers is devoted to this task with a special emphasis on the four phases highlighted in Fig. 1.

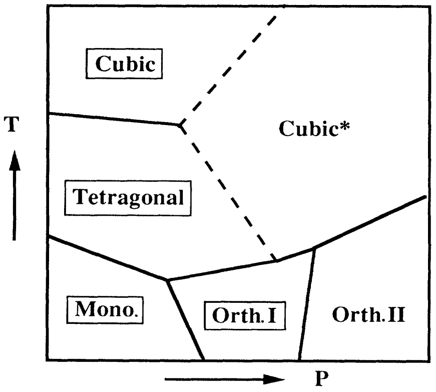

FIG. 1. Schematic *P-T* phase diagram of ZrO_2. The highlighted phases are studied in this work.

The four ZrO_2 polymorphs are closely related to the cubic fluorite structure, as shown in a simplified representation in Figs. 2(a)–2(e). Previous investigations of these structures were limited primarily to x-ray-, neutron-, and electron-diffraction studies (see Table I).[8-14] Although the diffraction data are highly reliable for pure ZrO_2 polymorphs, they cannot provide definitive information specific to the dopant and host cations for the two alloy phases. This limitation has greatly hampered the understanding of phase stability and dopant- and defect-related properties. This situation is particularly serious for tetragonal zirconia where we are unaware of any information on the local environment of dopants, based on diffraction data, having ever been reported. This is due to low dopant concentrations in this polymorph and the impossibility of obtaining single crystals (they undergo spontaneous and disruptive transformation during cooling). At any rate, since diffraction techniques are sensitive only to structural patterns that persist over a sufficiently long range, further studies of these important ceramic alloys using a more local and element-specific probe would be very worthwhile. The x-ray-absorption spectroscopy (XAS) technique can potentially provide such a probe.

Several investigations of zirconia systems using XAS

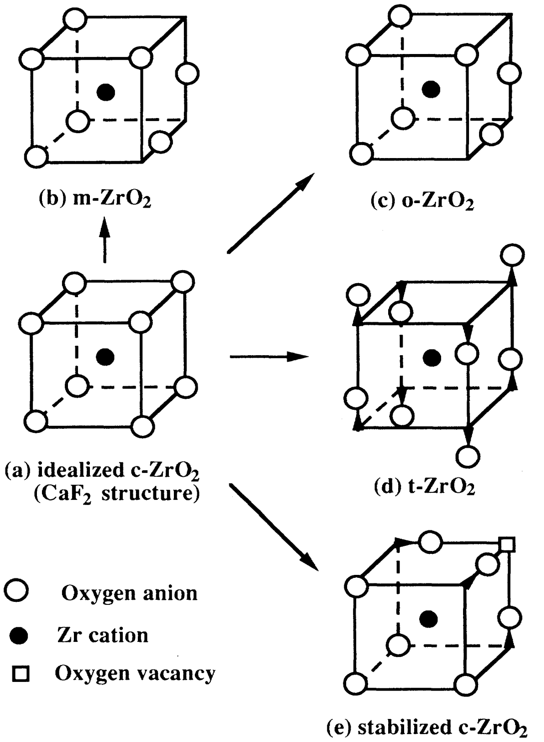

FIG. 2. (a) Schematic fluorite structure and (b)–(e) four related polymorphic distortions in ZrO_2.

have been reported in recent years, and they have begun to provide some new insight.[15–23] These studies, however, have only focused on dopants of large ionic sizes (for example, Y^{3+}, Gd^{3+}, Ce^{4+} and other rare-earth elements and on high dopant concentrations (cubic zirconia or pyrochlore-type zirconates). Therefore we have conducted a more systematic XAS analysis covering all four zirconia polymorphs with dopants of different ionic sizes and charges (Ga^{3+}, Fe^{3+}, Y^{3+}, Gd^{3+}, Ge^{4+}, Ti^{4+}, Ce^{4+}, and Nb^{5+}). By taking data at 10 K, Zr- and dopant-centered radial distribution functions, derived from extended x-ray-absorption fine structure (EXAFS), which extend to 9 Å in distance, have been obtained. Based on these results, we are able to obtain a comprehensive picture of the host and dopant environments in various solid solutions. In this paper, we report our new finding of characteristic Zr-XAS spectra [both EXAFS and x-ray-absorption near-edge structure (XANES)] which change very little with dopant and depend mainly on the polymorph. (This observation is believed to be general for host cations in all ionic solid solutions.) We describe the corresponding characteristic local structures around Zr and point out the similarities and differences between these pictures and those drawn by previous diffraction studies. Based on these results, insight into the atomistic origins of phase stability is provided.

II. EXPERIMENTAL PROCEDURES

A. Materials

Fine zirconia powders with various additives were synthesized by the following method. A solution was prepared by dissolving dopant oxides in hot dilute HNO_3 (or using a dopant-nitrate or dopant-ethoxide solution) and mixing this solution with $ZrOCl_2$ solution. Dilute NH_4OH was then added, with H_2O_2 and sugar as dispersants, to effect coprecipitation. The mixtures were dried at 200 °C and calcined at 650 °C to form zirconia solid solutions. Higher calcination temperatures were sometimes attempted after it was first verified that phase-pure

TABLE I. Crystallographic data of zirconia polymorphs.

Composition	Phase	Zr-O (Å)×N_{CN}[a]	Mean Zr-O (Å) and dispersion (Å)	Zr-Zr (Å)×N_{CN}[a]	Mean Zr-Zr (Å) and dispersion (Å)	Ref.
ZrO_2	monoclinic	2.051, 2.057, 2.151, 2.163, 2.189, 2.222, 2.285×1	2.160×7 (±0.085)	3.341×1, 3.433×2, 3.461×2, 3.463×1, 3.588×1, 3.923×2, 4.030×2, 4.540×1	3.720×12 (±0.366)	8
ZrO_2	orthorhombic	2.063, 2.110, 2.152, 2.187, 2.198, 2.200, 2.208×1	2.160×7 (±0.055)	3.418×2, 3.428×1, 3.515×1, 3.517×2,3.734×2, 3.776×2, 3.919×2	3.639×12 (±0.191)	9
ZrO_2	tetragonal (1250 °C)	2.065×4, 2.455×4	2.260×8 (±0.208)	3.64×4, 3.68×8	3.67×12 (+0.02)	10
$(Zr,Y)O_{1.97}$	tetragonal	2.08×4, 2.38×4	2.23×8 (±0.16)	3.61×4, 3.63×8	3.62×12 (±0.01)	12
ZrO_2	cubic (2400 °C)	2.28×8	2.28×8 (±0.00)	3.72×12	3.72×12 (±0.00)	13
$(Zr,Y)O_{1.87}$	cubic	2.04×3, 2.23×4 (O-relaxation model)	2.15×7 (±0.10)	3.64×12	3.64×12 (±0.00)	14
		2.05×3, 2.24×3, 2.41×1 (O- and Zr-relaxation model)	2.18×7 (±0.14)	3.49×3, 3.64×6, 3.79×3 (Zr shifts 0.18 along ⟨111⟩)	3.64×12 (±0.11)	14

[a] N_{CN} = coordination number.

TABLE II. Composition, calcination condition, and phase identification of samples.

Composition (mol % dopant oxide)	Calcination (°C)	Phase
Pure ZrO_2	1200	m^a
1 Y_2O_3	1300	m
5 CeO_2	1300	m
Pure ZrO_2	600, 6 GPa	o^a
12 CaO	1000	t
3 Y_2O_3	1300	t^a
6 Ga_2O_3	850	t
11 CeO_2	850 in O_2	t
10 TiO_2	850 in O_2	t
10 GeO_2	1000	t
10 Gd_2O_3	1300	c
20 Y_2O_3	1300	c^a

[a] XRD and EXAFS presented in Fig. 2 and Table III, respectively.

powders could still be obtained after such heat treatment. The metal oxide was used as the source for Y(III) and Gd(III), the nitrates were used for Ca(II), Ga(III), and Ce(IV), and the ethoxides were used for Ge(IV) and Ti(IV). The composition, calcination condition, and phase identification for all the samples are summarized in Table II. The orthorhombic zirconia powder was provided by Dr. Ohtaka of Osaka University who used a synthesis method to hold the powders at 600 °C and 6 GPa for 30 min before quenching to ambient condition.[24,25]

Phase identification and lattice parameter measurement were made by x-ray diffraction (XRD) using Cu $K\alpha$ radiation. A set of x-ray-diffraction patterns of four polymorphs obtained for pure ZrO_2 (monoclinic and orthorhombic), 3 mol % Y_2O_3-ZrO_2 (tetragonal), and 20 mol % Y_2O_3-ZrO_2 (cubic) are shown in Fig. 3. These powders will be referred to extensively in the subsequent XAS studies as representative of these four polymorphs.

B. X-ray-absorption measurements

X-ray-absorption measurements at the Zr K edge were made on Beamline 7-3 at the Stanford Synchrotron Radiation Laboratory. Energy selection was accomplished by using a double-crystal monochromator with Si(220) crystals. Detuning to 50% of the incident beam intensity at 1400 eV above the Zr K absorption edge was used to reduce the harmonic content of the beam. The absorption spectrum of pure monoclinic ZrO_2 was recorded as an energy calibration at the same time that the sample spectrum was recorded. The energies were calibrated by assigning the maximum inflection point of the Zr K edge in ZrO_2 as 17 998 eV. All spectra were measured at 10 K in transmission mode using ion chambers filled with argon gas. No detectable phase change occurred in these powders when they were cooled from room temperature to 10 K.

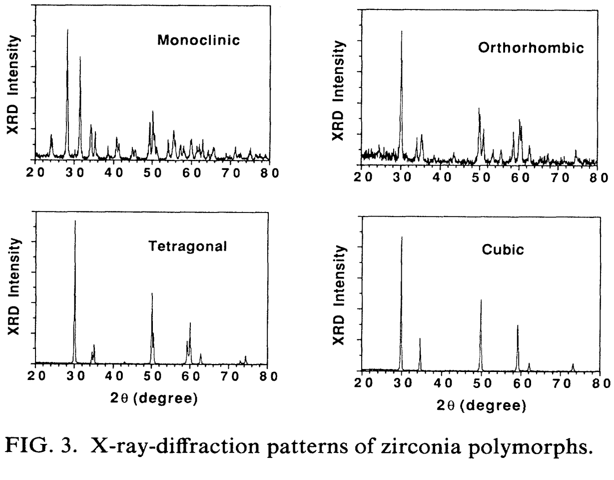

FIG. 3. X-ray-diffraction patterns of zirconia polymorphs.

The EXAFS spectra were analyzed using the standard EXAFS equation[26]

$$\chi(k)=\sum_j \frac{N_j}{kR_j^2}F_j(k)e^{-2\sigma_j^2k^2}e^{-2R_j/\lambda}\sin[2kR_j+\phi_j(k)]\;, \tag{1}$$

where $F_j(k)$ is the backscattering amplitude from each of the N_j neighboring atoms of the jth type at distance R_j with a mean-square relative displacement σ_j^2 and $\phi_j(k)$ is the total phase shift experienced by the photoelectron which includes contributions from both the scatterer and absorber. The factor $\exp(-2R_j/\lambda)$ accounts for inelastic scattering, where λ is the photoelectron mean free path. The photoelectron wave vector is related to the photon energy E by

$$k=\sqrt{8\pi^2m(E-E_0)/h^2}\;. \tag{2}$$

The threshold energy value E_0 was initially assigned as 18 015 eV for the Zr K edge. Data reduction followed standard procedures for pre-edge background subtraction and EXAFS background removal.[26] Fourier-filtered window values used for each shell of the polymorphs are given in Table III.

Our data-fitting procedure began with the assumption of Zr-O (8×2.22 Å^2) and Zr-Zr (12×3.625 Å^2) coordination numbers and distances from Shannon's table for ionic radii.[27] We then calculated the scattering amplitudes and phase-shift functions using the FEFF program (version 3.0) with a scale factor of 0.85–0.9.[28] Since the interatomic distance and fitting parameter E_0 are highly correlated, E_0 values were chosen so that the Zr-O distance of 2.16 Å and the first Zr-Zr subshell distance of 3.47 Å in m-ZrO_2 were reproduced, respectively. The optimum E_0 was 18 034 eV for the Zr-O shell and 18 039 eV for the Zr-Zr shell. These values for E_0 were then used in all subsequent data analysis, while the bond distance R, coordination number N_{CN}, and bond dispersion σ^2 were adjusted to obtain the best fit to the experimental data of unknown samples. Since N_{CN} and σ^2 are also highly correlated, we usually allow them to float first to obtain rough values; then, N_{CN} is fixed at a reasonable integer in order to compare σ^2 with each other. In some cases, if a single bond distance did not give a good fit, then a second distance (a two- or three-shell model) was introduced. The latter fitting results are reported if they

TABLE III. Fitting results of Zr, EXAFS for zirconia polymorphs.[a]

	Zr-O						Zr-Zr					
Polymorphs	ΔR_{filt} (Å)	Δk (Å^{-1})	R (Å)	N_{CN}	σ^2 (Å^2)	ρ (%)[b]	ΔR_{filt} (Å)	Δk (Å^{-1})	R (Å)	N_{CN}	σ^2 (Å^2)	ρ (%)[b]
Monoclinic	1.0–2.0	3–13	2.16	7.0	0.0100	5.8	2.5–4.5	3–17	3.46	7.0	0.0036	4.0
									4.01	4.0	0.0060	
									4.55	1.0	0.0024	
Orthorhombic	1.0–2.0	3–13	2.17	7.0	0.0066	1.7	2.5–4.0	3–17	3.47	6.0	0.0034	1.4
									4.01	4.0	0.0018	
									4.55	2.0	0.0013	
Tetragonal	1.0–2.1	3–17	2.10	4.0	0.0034	2.3	2.7–3.7	3–17	3.62	12.0	0.0034	0.3
			2.33	4.0	0.0090							
Stabilized cubic	0.9–1.9	3–13	2.15	7.0	0.0074	2.9	2.4–3.4	3–17	3.55	12.0	0.0090	1.4

[a] Fixed N_{CN}.

[b] Relative deviation between experimental data and calculated EXAFS. $\rho=\sum(k^3\chi_{\text{expt}}-k^3\chi_{\text{calc}})^2/\sum(k^3\chi_{\text{expt}})^2$.

are considerably better or much more reasonable than the single-shell fitted results. (All of the fitting results for R and N_{CN} obtained from this procedure are in good agreement with the results obtained by using empirical amplitude and phase functions derived from a model compound—pure m-ZrO_2. Using the latter procedure, however, we can only obtain a relative Debye-Waller factor $\Delta\sigma^2$ with reference to m-ZrO_2 and thus lose some of the structural information that is otherwise available from EXAFS.) The Zr-cation scattering is treated as Zr-Zr scattering in this work when the dopant concentration is low. The high concentration data analysis is limited to Y dopant only since Y and Zr have nearly identical scattering functions.

For analysis of the XANES data, the spectra were normalized by first subtracting a single, third-order polynomial from the data. The result was then multiplied by a scale factor. Since XANES theory is not developed enough to allow routine fitting of the experimental data, only qualitative interpretations based on some currently accepted empirical notions are presented.

III. RESULTS

A. Characteristic Zr EXAFS

Representative EXAFS spectra for the Zr K edge of several tetragonal compositions are shown in Fig. 4. These spectra are almost indistinguishable from each other, suggesting that they all correspond to the same characteristic spectrum of the tetragonal phase, regardless of the dopant used. Similarly, we present Zr EXAFS spectra of several monoclinic and cubic compositions in Figs. 5 and 6, respectively. Again, the spectra are almost indistinguishable within a single phase and may be regarded as characteristic spectra for these phases.

These three characteristic spectra and also that of o-ZrO_2 are compared in Fig. 7. We see very clear differences in their amplitudes, frequencies, and phase shifts. These differences can be more readily appreciated in their Fourier transforms (FT's), shown in Fig. 8. According to EXAFS theory,[26] the FT is related to the radial distribution function (RDF) around Zr with a phase shift α. They contain clearly resolvable structural infor-

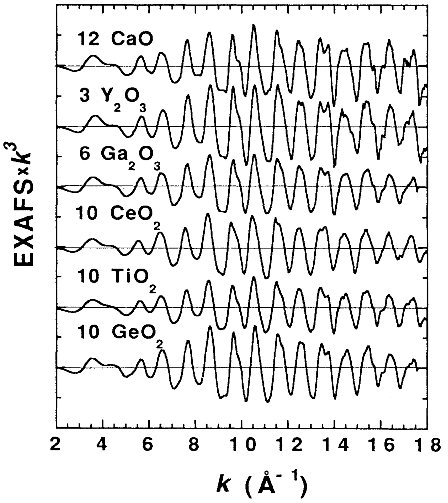

FIG. 4. EXAFS spectra of Zr K edge for tetragonal zirconia.

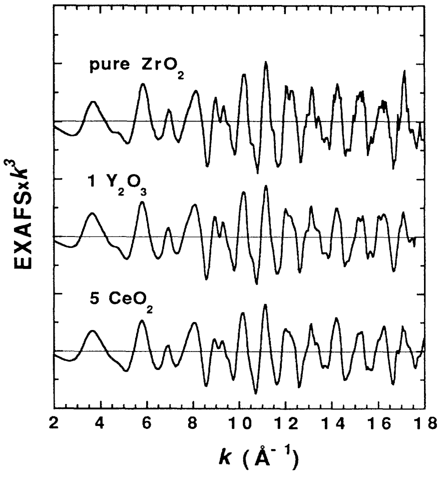

FIG. 5. EXAFS spectra of Zr K edge for monoclinic zirconia.

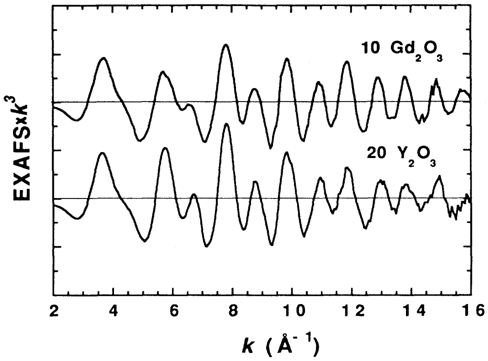

FIG. 6. EXAFS spectra of Zr K edge for dopant-stabilized cubic zirconia.

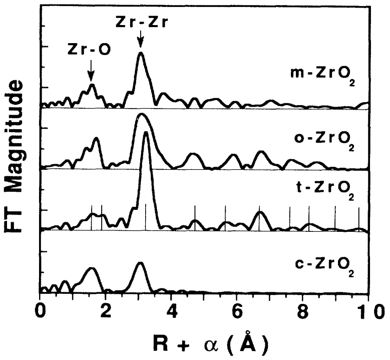

FIG. 8. Fourier transforms of Zr EXAFS for zirconia polymorphs.

mation out to at least 9 Å for monoclinic, orthorhombic, and tetragonal zirconia. This sensitivity is far better than most XAS data on similar ceramic samples reported in the literature.[15-23,29] Once again, it is apparent that Zr ions in different zirconia structures have very different RDF's. These differences are discussed below.

To begin with, we note that the first peak in the FT (Fig. 8) corresponds to the nearest neighbors (NN's) of the Zr ion, i.e., a Zr-O shell. The second peak corresponds to the next-nearest neighbors (NNN's), i.e., a Zr-Zr shell in pure zirconia or a Zr-cation shell in solid solutions. All of the higher-order peaks probably correspond to the outer Zr-Zr shells since the outer Zr-O shells are not expected to be observable due to the weak scattering function of oxygen. The major peaks in t-ZrO$_2$ are identified with bars in Fig. 8. Comparison of the number and relative intensity of the FT peaks reveals the following features. First, the NN Zr-O peaks in the m-, o-, and c-ZrO$_2$ polymorphs appear similar, while this peak in t-ZrO$_2$ is broader and weaker. This suggests similar Zr-O bonding in the former and different bonding in the latter. Second, the NNN Zr-Zr peak in t-ZrO$_2$ is singularly sharp and strong. This will be later attributed to the fact that cations in t-ZrO$_2$ are in a simple, nearly face-centered-cubic (fcc) arrangement, while cations in other polymorphs all have severe distortions. Third, the NNN as well as higher-order Zr-Zr peaks of c-ZrO$_2$ are very weak. The cubic zirconia solid solution used here contains 20 mol % Y$_2$O$_3$. However, since Y has nearly the same scattering behavior as Zr, the low amplitude must be caused by structural disorder in c-ZrO$_2$. Fourth, the amplitudes of the outer Zr-Zr peaks in t-ZrO$_2$ are, with the exception of the peak at 6.7 Å, surprisingly weak, despite the strongest NNN peak. This suggests that the photoelectron scattering in t-ZrO$_2$ is less coherent from Zr center to Zr center beyond NNN's. Finally, the peak at 6.7 Å in t-ZrO$_2$ is surprisingly strong. As will be discussed later, this may be attributed to multiple scattering which takes place between a colinear array of scatterers. In the next section, quantitative analysis of these characteristic EXAFS spectra will be presented to substantiate and elaborate the above observations. (See Table III. Graphs that illustrate the fit between theory and experiment are available from the authors.)

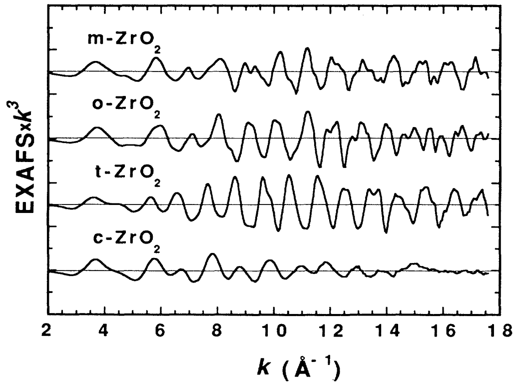

FIG. 7. EXAFS spectra of Zr K edge for zirconia polymorphs.

B. Quantitative analysis of NN Zr-O and NNN Zr-Zr shells

1. Monoclinic ZrO$_2$

The structure of m-ZrO$_2$ is best understood since it is available in pure single-crystal form (baddeleyite) at room temperature. Therefore we have used the diffraction data listed in Table I and Ref. 8 to calculate the EXAFS and FT and to clarify the interpretation of the EXAFS-derived characteristic structure. Calculations were performed using the FEFF program (version 5.04) for O and Zr atoms within 4.6 Å from the Zr absorber. The calculated FT's, at $\sigma=0$, are shown in Fig. 9 ($k=3-17$ Å^{-1}). It can be seen that the scattering contributions of Zr-O and Zr-O-Zr to the "second shell" between 2.5 and 4.5 Å are very small. The single-scattering calculation essentially reproduces all the basic features of the experimentally measured spectrum (Fig. 8). These include the relative peak positions and relative peak heights. The discrepancy in the absolute peak positions and heights is due to the different choices for E_0 and σ (both set to 0 in the calculation). These values can be adjusted as fitting parameters to obtain an excellent fit with experimental data. However, such a fit is rendered meaningless because of the large number of fitting parameters (38 in to-

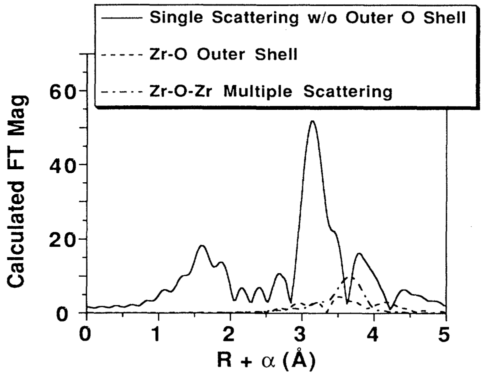

FIG. 9. Calculated Fourier transforms of Zr EXAFS from FEFF code for m-ZrO_2. "Zr outer shell" is from scattering of oxygens between 3.6 and 4.6 Å. "Zr-O-Zr multiple scattering" is from 47 three-atom scattering paths. The solid curve is from single scattering of inner-shell oxygens (2.0–2.9 Å) and single scattering of Zr (3.3–4.6 Å).

tal for the Zr-O first shell and Zr-Zr second shell, without accounting for multiple scattering and outer Zr-O scattering) made necessary by the very broad distribution of bond distances in this low-symmetry structure. More significantly, the essential agreement between the experimentally measured spectrum and the theoretically calculated one based on diffraction data indicates that the characteristic EXAFS spectrum indeed reflects the characteristic local structure around Zr.

As noted above, the Zr-O and Zr-Zr distributions are obviously too broad to be regarded as single shells. For future reference and comparison, however, we nevertheless choose to regard the FT between 1.0 and 2.0 Å as the first (Zr-O) shell and that between 2.5 and 4.5 Å as the second (Zr-Zr) shell. The latter is fit by three subshells. The fitting results, shown in Table III, are in good agreement with crystallography. The obtained bond distance for the Zr-O shell agrees with the crystallographic mean distance of 2.16 Å (see Table I). The first Zr-Zr subshell has a distance of 3.47 Å (×7) which is identical to the mean distance of the first seven Zr-Zr pairs in Table I. Likewise, the second Zr-Zr subshell has a distance of 4.01 Å (×4) which is nearly the same as the mean distance of the next four Zr-Zr pairs in Table I (4.00 Å). Last, the third Zr-Zr subshell has a distance of 4.55 Å (×1) which also coincides with the remaining single Zr-Zr pair in Table I. Overall, it appears that our choice for the subshells is justifiable at least for the purpose of reference and comparison.

2. *Orthorhombic ZrO_2*

No prior XAS data on orthorhombic zirconia has been reported. We found that the signal-to-noise ratio was remarkably good in this case, so that structural features up to 9 Å could be clearly distinguished. Quantitative analysis follows the same procedure as in the case of m-ZrO_2. Again, there is a sevenfold-coordinated Zr-O polyhedron with a slightly longer average bond distance of 2.17 Å. However, comparison of σ^2 for o-ZrO_2 and m-ZrO_2 shows a smaller distortion. Analysis of the Zr-Zr shell leads to a three-shell model: 3.47 Å×6, 3.78 Å×4, and 3.93 Å×2. These distances (Table III) are in good agreement with the crystallographic data if appropriate grouping is chosen from Table I. The triple Zr-Zr shell in o-ZrO_2 is similar to the case in m-ZrO_2, although the average Zr-Zr distance and the spread in Zr-Zr distance are both smaller in o-ZrO_2. This can be understood if we recall the suggestion of Chiao and Chen[30] and Ohtaka *et al.*[9] that the orthorhombic unit cell can be approximately modeled, other than a contraction along the [001] axis, as two monocline unit cells inverted to follow a (100) twin relation.

3. *Tetragonal ZrO_2 solid solutions*

Quantitative analysis of the Zr-O peak for 3 mol % Y_2O_3-ZrO_2 using a single-shell model gives an N_{CN} of around 2 at 2.10 Å. This is chemically unreasonable. Therefore a two-shell model was employed to fit the Zr-O shell which produced much better results (see Fig. 10). The two sets of distances obtained were 2.10 and 2.33 Å. The origin of this splitting is evident from Fig. 2(d). The second (Zr-Zr) peak can be fit successfully by a single-shell model with an N_{CN} of 12 at 3.62 Å.

We have also obtained a quantitative fitting for all the tetragonal Zr EXAFS of Fig. 4. The results are summarized in Table IV. Similar results are obtained for all six samples. The Zr-O bond lengths are 2.09–2.10 Å×4 and 2.33–2.35 Å×4, and the Zr-cation distances are between 3.61 and 3.63 Å. Since variations of this magnitude are within the resolution of the technique and distances obtained from EXAFS are highly reliable, this similarity confirms that the Zr-centered RDF is indeed independent of the dopant kind and size.

A simple calculation can be used to identify all the major peaks up to 9 Å in Fig. 8 for t-ZrO_2. We can calculate the theoretical Zr-centered RDF for an idealized tetragonal zirconia structure [$P4_2/nmc$, with oxygen position parameter $z(4d)=0.21$ (Refs. 12 and 31)] using the mea-

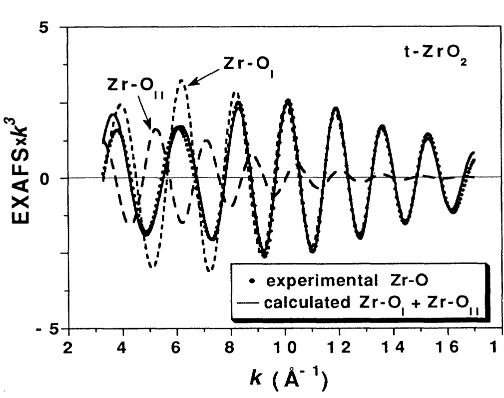

FIG. 10. Comparison between EXAFS data and two-shell model for Zr-O in ZrO_2. Calculated subshell contributions shown as dashed and dotted curves and their sum as the solid curve.

TABLE IV. Fitting results of Zr EXAFS for doped tetragonal zirconia.[a]

Composition (mol % dopant oxide)	Zr-O R (Å)	Zr-O N_{CN}	Zr-O σ^2 (Å^2)	Zr-Zr R (Å)	Zr-Zr N_{CN}	Zr-Zr σ^2 (Å^2)
12 CaO	2.09	4.0	0.0037	3.62	12	0.0036
	2.33	4.0	0.0098			
3 Y_2O_3	2.10	4.0	0.0034	3.62	12	0.0034
	2.33	4.0	0.0090			
6 Ga_2O_3	2.09	4.0	0.0040	3.62	12	0.0042
	2.33	4.0	0.0110			
11 CeO_2	2.10	4.0	0.0035	3.63	12	0.0040
	2.35	4.0	0.0096			
10 TiO_2	2.09	4.0	0.0041	3.63	12	0.0050
	2.33	4.0	0.0114			
10 GeO_2	2.09	4.0	0.0041	3.61	12	0.0035
	2.34	4.0	0.0110			

[a] Fixed N_{CN}.

sured lattice parameters ($a = 5.1060$ Å and $c = 5.1808$ Å). This is shown in Fig. 11 with the oxygen neighbors after 4.5 Å omitted. The calculated RDF has a split Zr-O shell with bond lengths of 2.10 and 2.33 Å, in agreement with the fitting values. The fitted Zr-cation distance of 3.62 Å×12 is also consistent with the calculated Zr-Zr distances (3.61 Å×4 and 3.63 Å×8). Next, comparing the position of the second peak in Fig. 8 with the fitted Zr-Zr distance, we estimate the phase shift α to be 0.5 Å. We then find that the positions of all the higher-order peaks coincide with the calculated Zr-Zr pair distances, particularly those marked as 2, 3, 4, and 6, and identified by marker lines in Fig. 8. The absence of peak 5 is probably because of the relatively large distance dispersion in this peak due to tetragonality, while the absence of peaks 7 and 8 is because of their longer distances. Overall, the excellent correspondence provides a direct confirmation that the cation arrangement in t-ZrO_2 is indeed nearly fcc. It also demonstrates unambiguously that RDF's up to 9 Å can be resolved from XAS. Finally, the anomaly at 6.7 Å, marked as 4, corresponds to the face-diagonal Zr-Zr pairs (12 in total). It arises because there is an intervening scatterer which is nearly collinear with the absorber, giving an amplitude enhancement due to favorable forward scattering of photoelectrons.[26] This is expected to occur for face-diagonal arrays for the fcc ions. The observation of this "focusing effect" is thus another indication that the Zr-cation lattice is nearly fcc.

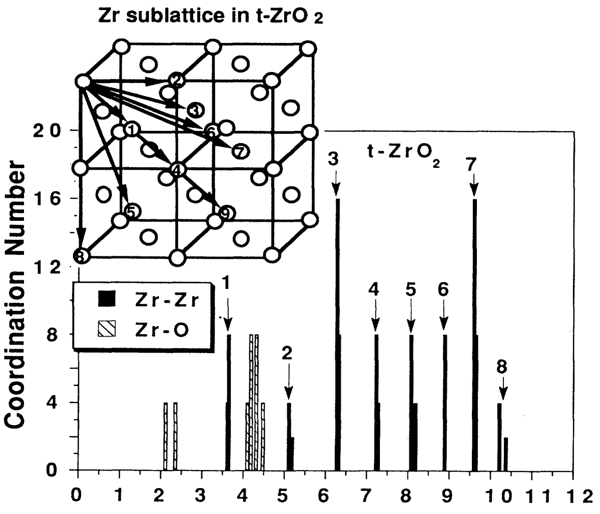

FIG. 11. Calculated Zr-centered radial distribution function for t-ZrO_2 (oxygen shells after 4.5 Å are omitted). Zr atoms are shown in a tetragonally distorted fcc lattice in the inset in which all arrows originate from the corner atom. Doublets at most peaks are due to tetragonality.

4. Cubic ZrO_2-Y_2O_3 solid solution

The Zr-O shell in c-ZrO_2 (20 mol % Y_2O_3) is very similar to that in m- and o-ZrO_2, both in bond distance and in coordination number, and totally unlike that in t-ZrO_2 (see Table III). While this may initially seem surprising in view of symmetry and unit-cell geometry, it is actually consistent with the structural picture depicted in Fig. 2 where oxygen vacancies and displacement are considered. Within the resolution of EXAFS, the Zr-O shell data are also consistent with both O-relaxation and O-cation-relaxation models in Table I where crystallographic data are listed. In contrast, the EXAFS and crystallographic results for the NNN Zr-cation shell do not agree. The EXAFS distance of 3.55 Å is much smaller than the 3.64 Å estimated by assuming either model (the measured lattice parameter $c = 5.1748$ Å). Surprisingly, EXAFS for the cubic phase, 3.55 Å, is actually shorter than that in the tetragonal structure (3.62 Å), although Zr in both cases have the same 12-fold cation coordination.

An apparent shell contraction can arise from an asymmetric distortion which is more severe at the larger radial distance than the mean; the resultant FT using the Gaussian distribution model for the bond distribution is then weighted in favor of the shorter distances. This may be a cause of the apparent contraction observed in the Y-stabilized c-ZrO_2. This is consistent with the much larger value of σ^2 seen for this shell. As noted before, the

FT for c-ZrO_2 shows a much lower amplitude for the NNN Zr cation and for the higher-order peaks as compared with other polymorphs (Figs. 7 and 8). We believe this is due to a distortion of the cation network that washes out the high-R features in the RDF, and therefore we rule out the O-relaxation-only model since it does not allow cation displacement.

C. Characteristic Zr XANES

Representative XANES spectra for the four polymorphs and their corresponding first derivatives are shown in Figs. 12 and 13, respectively. They are again independent of the type of the dopant and may be regarded as characteristic of the respective structures. There is no detectable edge shift among the spectra. This is consistent with the notion that the valence of Zr in these samples remains the same and that a similar covalency prevails. More subtle differences, however, do exist. Turning first to the edge width, which is commonly defined as the full width at half maximum of the main peak in the first derivative, we find a decreasing edge width from monoclinic and orthorhombic to cubic and tetragonal spectra. The edge width can be used to determine the width of the valance band, which is a measure of splitting of the degenerate energy levels and an indicator of the absorber symmetry.[32,33] For highly symmetric coordinations, the edge width should be small. Conversely, it should be large for highly distorted coordinations. Thus the Zr-O coordination is more symmetric in t-ZrO_2 and c-ZrO_2 than in m- or o-ZrO_2. An alternative explanation follows the empirical correlation[32] that an increase in the edge width corresponds to an increase in the overall covalent character of the metal-ligand bond for the same symmetry. Thus the larger edge width in o- and m-ZrO_2 is an indication of their higher covalency. This conclusion is supported by a recent band-gap calculation[34] which shows a wider gap in m-ZrO_2 than in t-ZrO_2. Both distortion and covalency changes are likely to be present, although their relative contribution is difficult to assess at this point.

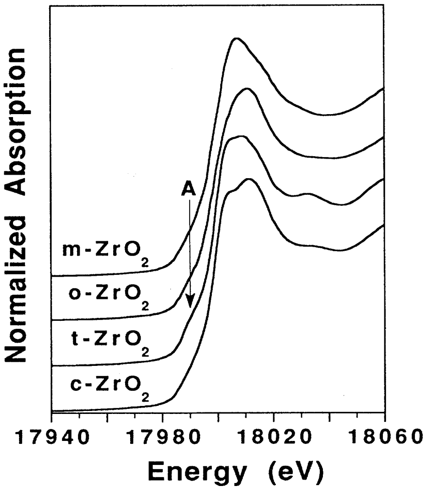

FIG. 12. XANES spectra of Zr K edge for zirconia polymorphs. $1s \rightarrow 4d$ shoulder marked as A.

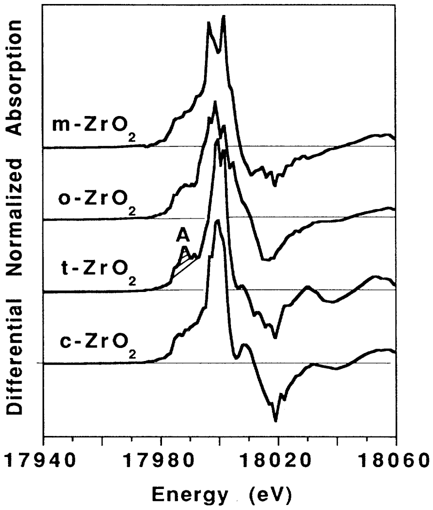

FIG. 13. First derivative of Zr XANES for zirconia polymorphs. $1s \rightarrow 4d$ shoulder hatched and marked as A.

Another observation is a small shoulder about 6–7 eV beyond the Zr K-edge threshold which is most apparent in the tetragonal spectrum (peak A in Fig. 12). This is more evident in the first derivative plot of Fig. 13 where the feature is marked by hatches. In general, XANES features within ~ 10 eV of the edge threshold are due to electronic transitions to unoccupied high-energy states near the Fermi level and are sensitive to the local geometry of the probe atom. Thus the observation that peak A is well resolved only in t-ZrO_2 is another indication of the different Zr-O geometry in this polymorph. As suggested from the electron-energy-loss spectroscopy of ZrO_2,[35] the shoulder at 7 eV can be attributed to a $1s \rightarrow 4d$ transition, which is forbidden unless some d-p mixing is operating. As for the $1s \rightarrow 3d$ transition in first-row transition metals, the intensity of the $1s \rightarrow 4d$ feature will be stronger in compounds that are distorted from centrosymmetry.[36,37] More specifically, the Zr-O geometry in t-ZrO_2 can be regarded as two sets of nonequivalent Zr-O tetrahedra. Since tetrahedral geometries are known to enhance d-p mixing relative to that seen for sevenfold coordination, the stronger transition in t-ZrO_2 is understandable. Similarly, as the structure approaches octahedral coordination, as in pyrochlore structure,[23] this shoulder becomes even weaker than it is in c- and m-ZrO_2.

IV. DISCUSSION

A. Zr-O bonding

A basic feature of Zr-O bonding is its strong covalent character, as emphasized by Ho,[38] making it unsuitable to adopt a fluorite-type eightfold coordination. This is evident considering the rather small ionic radius of Zr^{4+}. The consequence of this is well known and is manifested in the sevenfold coordination of Zr-O found in m-ZrO_2.

EXAFS has shown such Zr-O bonding with essentially identical R and N_{CN} in three polymorphs, m-, o-, and c-ZrO_2. For these polymorphs, the similarity is also found in XANES, particularly in the weak $1s \rightarrow 4d$ features.

In order for the Zr-O polyhedra in nominally fluorite-structured c-ZrO_2 to attain a coordination similar to that in m- and o-ZrO_2, oxygen vacancies due to dopants are needed. The large variety of possible configurations of dopants and vacancies distributed in the host lattice and the attendant local relaxations have the effect of "randomizing" the Zr-O bonding, resulting in a large multiplicity of Zr sites with low local symmetry.[39] The extent of "randomness" or "glassiness" may be quantified by the Debye-Waller factor. At 10 K, the bond dispersion in c-ZrO_2 with 20 mol % Y_2O_3 is 0.0074 Å^2 between that in m-ZrO_2 (0.0100 Å^2) and o-ZrO_2 (0.0066 Å^2).

Unlike the other polymorphs, Zr-O bonding in t-ZrO_2 has nominally eightfold coordination. As with $ZrSiO_4$ and $ZrGeO_4$, the undersized Zr is able to take up the ZrO_8 polyhedron only by distorting it into two tetrahedra. Although the oxygens are labeled as O_{I} and O_{II} in the space group of $P4_2/nmc$,[10] they are crystallographically indistinguishable in a perfect lattice and in the diffraction concept. We are able, however, to resolve the two Zr-O distances and, equally significantly, the two different Debye-Waller factors. This is important because the t-ZrO_2 can be alternately viewed as a layered structure.[10] Referring to Fig. 2(d), we may picture the O_{I} to form a smaller flattened tetrahedron on the plane and the O_{II} to form an elongated tetrahedron between the plane. (The resultant configuration is similar to the more covalent and layerlike HgI_2 compound.[40]) The interlayer O_{II} ions can then be viewed as rather loosely bound and subject to large static and thermal distortion. This bonding difference is justified even for perfect t-ZrO_2 structure at 0 K according to the recent total-energy calculations by Jansen.[41] He found that each Zr^{4+} ion is strongly bonded to only four NN oxygens, O_{I}, and that the large bond strength difference between Zr-O_{I} and Zr-O_{II} is manifested by their very different electron densities.

B. Zr-cation bonding

Of all the polymorphs studied here, the tetragonal structure has the most regular Zr-cation arrangement. Since the small tetragonal distortion is undetectable by EXAFS, the cation-cation distances obtained from EXAFS are in good agreement with the values calculated for a fcc lattice. The very strong focusing enhanced peak for face-diagonal cation pairs also confirms the same. However, the relatively low amplitudes of the other higher-order Zr-cation peaks in t-ZrO_2, compared with those of o-ZrO_2, are interesting. It may be indicative of the instability of the Zr-cation network in the t-ZrO_2 structure. Such instability would be expected to lead to softer vibrational modes in t-ZrO_2, with consequently weaker EXAFS scattering beyond a correlation length (~7 Å), even at 10 K. This has been confirmed by temperature-dependent EXAFS data described in a subsequent paper.

There are obviously several distortions in the dopant-stabilized c-ZrO_2 despite its fluorite-type Bragg reflections indicating higher symmetry. They are manifested in the very low amplitude of the NNN Zr-cation peak and the disappearance of all higher-order peaks (Fig. 8). In addition, the apparent contraction of the NNN Zr-cation distance is probably due to a non-Gaussian distribution of bond distances in the highly distorted structure. If we allow the central Zr ion to shift 0.18 Å along the ⟨111⟩ direction, as proposed by Steel and Fender in their neutron-diffraction study (12 mol % Y_2O_3),[14] we obtain the following Zr-cation distances: 3.49 Å×3, 3.79 Å×3, and 3.64 Å×6. The mean-square deviation (σ^2), 0.0111 Å^2, is close to the experimentally measured value of 0.0090 Å^2 for the stabilized c-ZrO_2 with 20 mol % Y_2O_3. Thus the O-cation-relaxation model[14] is supported by our data. Note, however, that diffraction studies cannot differentiate between host and dopant cations, which actually have very different distortions depending on the relative size and charge of the dopants, as will be demonstrated in future publications.

C. Characteristic local structures

The characteristic local structures we identified are explicable only if dopant cations cause very small perturbation to their surrounding. We have recently summarized the local structures of dopant cations (M) in tetragonal and cubic zirconia solid solutions, and the results are reproduced in Table V.[42] It is remarkable that, regardless of their disparate coordination number (from 4 to 8) and bond distance (from 1.81 to 2.38 Å) for the first shell, all the dopants have a similar dopant-cation distance for the second shell, 3.61–3.63 Å. The latter distance is essentially the same as the Zr-Zr distance in t-ZrO_2 which most closely resembles the fluorite structure. Thus the perturbation caused by dopant cations is a short-range one and is already much damped at the distance of the second shell. This, in turn, allows the host cations to assume their phase-dependent characteristic structures despite the presence of the dopants. Recognizing this feature, we have recently used host cation EXAFS to identify phases in ultrafine powders for which Bragg reflections are too broad to resolve peak splitting.

The reason for the rapid damping of the dopant's per-

TABLE V. EXAFS results of M-O and M-cation distances.

Composition	Phase	M-O	R (Å)	M-cation (Å)
Zr(Gd)$O_{1.91}$	c	Gd-O	2.38	3.62
Zr(Gd)$O_{1.97}$	t	Gd-O	2.38	3.62
Zr(Y)$O_{1.91}$	c	Y-O	2.33	3.62
Zr(Y)$O_{1.97}$	t	Y-O	2.33	3.62
Zr(Fe)$O_{1.97}$	t	Fe-O	2.01	
Zr(Ga)$O_{1.97}$	t	Ga-O	1.93	
Zr(Ce)O_2	t	Ce-O	2.30	3.63
Zr(Ge)O_2	t	Ge-O	1.81	3.61
Zr(Y,Nb)O_2	t	Y-O	2.32	3.62
Zr(Y,Nb)O_2	t	Nb-O	1.90	3.61

turbation can be partly understood from the continuum elasticity theory. Treating the dopant as a point source of expansion or contraction, we predict the radial displacement at a distance r from the point source to decay as r^{-2}.[43] For a fluorite structure, the ratio of M-O and M-cation distance is $(\frac{3}{8})^{1/2}$, and so the displacement at the second shell is only $\frac{3}{8}$ of that at the first shell. Thus the rapid decay of dopant perturbation is understandable. (The actual value of displacement seems even smaller than the above estimate. This is likely due to the relative "softness" of oxygens, which are more deformable than the rigid-sphere cations.)

The characteristic spectra do change outside of the experimental error from system to system. These changes are related to the dopant size, charge, and their distribution (ordering). XAS is once again ideally suited for such a study. A discussion of this aspect is beyond the scope of the present paper and will be undertaken in future publications.

D. Implications for phase transformation

Based on the space groups, we would expect a progressive distortion of the local structure, as the symmetry changes from cubic to tetragonal to orthorhombic to monoclinic. Our results suggest a different picture. The distortion of both the NN and NNN shells, as judged by EXAFS, increases from tetragonal to orthorhombic to cubic to monoclinic phases. This can be seen for Zr-O distortion by comparing their Debye-Waller factors (Table III). The same sequence of distortion also holds for the Zr-cation network. (For pure oxide, we calculate σ^2 for the Zr-Zr shell from Table I as 0.134 Å^2 for m-ZrO_2 and 0.037 Å^2 for o-ZrO_2. For solid solutions, the σ^2 values from Table III are 0.0034 Å^2 for t-ZrO_2 and 0.0090 Å^2 for c-ZrO_2.) Thus it is the latter that coincides with the sequence of thermodynamic stability. This observation confirms that ZrO_2 structure requires distortions to gain stability, a viewpoint well founded in crystal chemistry but thus far obscured by the symmetry–space-group consideration.

The root of zirconia instability lies in the small ionic radius of Zr^{4+} which makes it unfavorable to adopt the eightfold coordination required for fluorite structure. Distortions of both Zr-O and Zr-cation shells are thus needed. Note that little volume change is involved in the transition among c-, t-, and o-ZrO_2, but transformation to m-ZrO_2 involves a substantial volume increase, ~4%.[8–14] This implies that the main distortions in the former case, the distortion of the NN Zr-O bonds, and the progressive distortion of the NNN Zr-Zr bonds are isovolumetric, whereas the distortion of the NNN Zr-Zr bonds in m-ZrO_2 is responsible for the volume increase. It is a common observation in phase transformation that an isovolumetric distortion involves less energy than a density-changing transformation. Therefore relatively small energy differences exist between t-ZrO_2, o-ZrO_2, and dopant-stabilized c-ZrO_2, but a large energy change remains between them and m-ZrO_2. It is also clear that a change of Zr-O coordination alone is energetically insufficient to fully stabilize ZrO_2.

V. CONCLUSIONS

(1) The Zr EXAFS and XANES spectra for four zirconia polymorphs have characteristic features which are phase dependent but dopant independent. The perturbation caused by dopants is localized to the NN's and mostly damped at NNN's and beyond. This observation is suggested to be general for host cations in ionic solid solutions.

(2) The Zr-cation network in t-ZrO_2 is nearly fcc, but evidence points to its incoherent distortion beyond a correlation length (~ unit-cell size) even at 10 K because of phase instability. The Zr-O first shell is bifurcated into two tetrahedra with the outer O_{II} severely distorted.

(3) Zr-O bonding is similar in m-, o, and c-ZrO_2, with sevenfold coordination and comparable bond distance. Despite its fluorite-type of symmetry, the Zr-cation network in c-ZrO_2 is severely distorted to accommodate the sevenfold Zr-O polyhedra. High-order FT peaks are washed away because of the distortion.

(4) Overall, the distortion of both the Zr-O and Zr-Zr shells increases in the order of t-, o-, c-, and m-ZrO_2. While this order is not the same as that of global crystal symmetry, it coincides with that of increasing phase stability. Partial stabilization is achieved by adopting sevenfold coordination for Zr-O bonding without changing volume, but further stabilization requires a distorted and dilated cation network.

ACKNOWLEDGMENTS

We are grateful to Dr. Ohtaka (Osaka University) for providing the orthorhombic powder and to Dr. B. Hedman and J. deWitt (both SSRL) for experimental assistance. SSRL is funded by the U.S. Department of Energy with additional support from the U.S. National Institute of Health. This research is supported by the U.S. National Science Foundation under Grant No. DMR-9119598.

---

[1] G. Bocquillon and C. Susse, Rev. Int. Hautes Temp. Refract. **6**, 263 (1969).

[2] S. Block, J. A. H. Da Jornada, and G. J. Piermarini, J. Am. Ceram. Soc. **68**, 497 (1985).

[3] H. Arashi, O. Shimomura, T. Yagi, S. Akimoto, and Y. Kudoh, in *Science and Technology of Zirconia III*, edited by S. Sōmiya, N. Yamamoto, and H. Hanagida, Advances in Ceramics Vol. 24 (American Ceramic Society, Westerville, OH, 1988), pp. 493–500.

[4] *Science and Technology of Zirconia I*, edited by A. H. Heuer and L. W. Hobbs, Advances in Ceramics Vol. 3 (American Ceramic Society, Westerville, OH, 1981).

[5] *Science and Technology of Zirconia II*, edited by N. Claussen, M. Rühle, and A. H. Heuer, Advances in Ceramics Vol. 12 (American Ceramic Society, Westerville, OH, 1984).

[6] *Science and Technology of Zirconia III*, edited by S. Sōmiya, N. Yamamoto, and H. Yanagina, Advances in Ceramics Vols. 24A and 24B (American Ceramic Society, Westerville, OH,

1988).

[7] *Zirconia V,* edited by S. P. S. Badwal, M. J. Bannister, and R. H. J. Hannink (Australian Ceramic Society, Melbourne, 1992).

[8] D. K. Smith and H. W. Newkirk, Acta Crystallogr. **18**, 983 (1965).

[9] O. Ohtaka, T. Yamanaka, S. Kume, N. Hara, H. Asano, and F. Izumi, Proc. Jpn. Acad. B **66**, 193 (1990).

[10] G. Teufer, Acta Crystallogr. **15**, 1187 (1962).

[11] P. Aldebert and J. P. Traverse, J. Am. Ceram. Soc. **68**, 34 (1985).

[12] D. Michel, L. Mazerolles, and M. Perez Y Jorba, J. Mater. Sci. **18**, 2618 (1983).

[13] D. K. Smith and C. F. Cline, J. Am. Ceram. Soc. **45**, 249 (1962).

[14] D. Steele and B. E. F. Fender, J. Phys. C **7**, (1974).

[15] C. R. A. Catlow, A. V. Chadwick, G. N. Greaves, and L. M. Moroney, J. Am. Ceram. Soc. **69**, 272 (1986).

[16] L. M. Moroney, Adv. Ceram. **23**, 649 (1987).

[17] M. H. Tuilier, J. Dexpert-Ghys, H. Dexpert, and P. Lagarde, J. Solid State Chem. **69**, 153 (1987).

[18] T. Uehara, K. Koto, S. Emura, and F. Kanamaru, Solid State Ion. **23**, 331 (1987).

[19] Y. Shimizugawa, H. Morikawa, F. Marumo, A. Nakajima, K. Urabe, and M. Normura, J. Jpn. Ceram. Soc. **95**, 1131 (1987).

[20] Z. J. Shen, T. K. Li, K. Q. Lu, and Y. Q. Zhao, J. Chin. Silic. Soc. **16**, 270 (1988).

[21] B. W. Veal, A. G. Mckale, A. P. Paulikas, S. J. Rothman, and L. J. Nowicki, Physica B **150**, 234 (1988).

[22] H. Morikawa, Y. Shimizugawa, F. Marumo, T. Harasawa, H. Ikawa, K. Tohji, and Y. Udagawa, J. Jpn. Ceram. Soc. **96**, 253 (1988).

[23] D. Komyoji, A. Yoshiasa, T. Moriga, S. Emura, F. Kanamaru, and K. Koto, Solid State Ion. **50**, 291 (1992).

[24] R. Suyama, T. Ashida, and S. Kume, J. Am. Ceram. Soc. **68**, C-314 (1985).

[25] O. Ohtaka, T. Iwami, K. Urabe, and S. Kume, J. Am. Ceram. Soc. **71**, C-164 (1988).

[26] B. K. Teo, *EXAFS: Basic Principles and Data Analysis* (Springer-Verlag, New York, 1986).

[27] R. D. Shannon, Acta Crystallogr. A **32**, 751 (1976).

[28] J. J. Rehr, J. Mustre de Leon, S. I. Zabinsky, and R. C. Albers, J. Am. Chem. Soc. **113**, 5135 (1988).

[29] P. Li, I-W. Chen, J. E. Penner-Hahn, and T. Y. Tien, J. Am. Ceram. Soc. **74**, 958 (1991).

[30] Y. H. Chiao and I-W. Chen, Acta Metall. Mater. **38**, 1163 (1990).

[31] W. W. Barker, F. P. Bailey, and W. Garrett, J. Solid State Chem. **7**, 448 (1973).

[32] U. C. Srivastava and H. L. Nigam, Coord. Chem. Rev. **9**, 275 (1973).

[33] J. C. J. Bart, Adv. Catal. **34**, 203 (1986).

[34] F. Zandiehnadem, R. A. Murray, and W. Y. Ching, Physica B **150**, 19 (1988).

[35] J. Frandon, B. Brousseau, and F. Pradal, Phys. Status Solidi B **98**, 379 (1980).

[36] J. E. Hahn, R. A. Scott, K. O. Hodgson, S. Doniach, S. R. Desjardins, and E. I. Solomon, Chem. Phys. Lett. **88**, 595 (1982).

[37] A. L. Roe, D. J. Scaneider, R. J. Mayer, J. W. Pyrz, J. Widom, and L. Que, Jr., J. Am. Chem. Soc. **106**, 1676 (1984).

[38] S. M. Ho, Mater. Sci. Eng. **54**, 23 (1982).

[39] J. Dexpert-Ghys, M. Faucher, and P. Caro, J. Solid State Chem. **54**, 179 (1984).

[40] A. F. Wells, *Structural Inorganic Chemistry,* 5th ed. (Clarendon, Oxford, 1986), p. 196.

[41] H. J. F. Jansen, Phys. Rev. B **43**, 7267 (1991).

[42] I.-W. Chen, P. Li, and J. E. Penner-Hahn, in *Application of Synchrotron Radiation Techniques to Materials Science,* edited by D. Perry, N. D. Shinn, R. L. Stockbauer, K. L. D'Amico, and L. J. Terminello, Materials Research Society Symposia Proceedings No. 307 (Materials Research Society, Pittsburgh, 1993), pp. 27–38.

[43] J. P. Hirth and J. Lothe, *Theory of Dislocations,* 2nd ed. (Wiley, New York, 1992), p. 49.